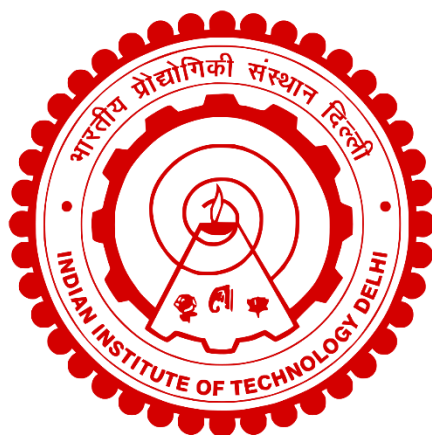


NEAR-FIELD COUPLED ASYMMETRIC TERAHERTZ METASURFACES AND THEIR APPLICATIONS

SUKHVINDER KAUR



**DEPARTMENT OF PHYSICS
INDIAN INSTITUTE OF TECHNOLOGY DELHI
NOVEMBER 2024**

© 2024, All Rights Reserved

Indian Institute of Technology Delhi (IITD), New Delhi-110016

NEAR-FIELD COUPLED ASYMMETRIC TERAHERTZ METASURFACES AND THEIR APPLICATIONS

by

SUKHVINDER KAUR

Department of Physics, IIT Delhi

Submitted

in the fulfillment of the requirements of the degree of Doctor of Philosophy

to the



INDIAN INSTITUTE OF TECHNOLOGY DELHI

NOVEMBER 2024

ੴ ਸਤਿ ਨਾਮੁ ਕਰਤਾ ਪੁਰਖੁ ਨਿਰਭਉ ਨਿਰਵੈਰੁ
ਅਕਾਲ ਮੂਰਤਿ ਅਜੂਨੀ ਸੈਭੰ ਗੁਰ ਪ੍ਰਸਾਦਿ ॥

There is one Supreme Being, the Eternal Reality, the Creator, without fear and devoid of enmity, immortal, never incarnated, self-existent, known by grace through the Guru.

Dedicated to my Family.....

CERTIFICATE

This is to certify that the thesis entitled “**Near-Field Coupled Asymmetric Terahertz Metasurfaces and their Applications,**” submitted by **Ms. Sukhvinder Kaur** to the Indian Institute of Technology Delhi for the award of “Doctor of Philosophy” is a record of the original, bonafide research work carried out by her under my supervision and guidance. The thesis has reached the standards fulfilling the requirements of the regulations related to the award of the degree. The results contained in this thesis have not been submitted in part or in full to any other University or Institute for the award of any degree or diploma to the best of my knowledge.



Dr. R. K. Varshney

Professor

Department of Physics

Indian Institute of Technology Delhi

New Delhi- 110016

India



Dr. Dibakar Roy Chowdhury

Professor

Department of Physics

Mahindra University

Telangana- 500043

India

ACKNOWLEDGEMENT

To begin with, I would like to extend my heartfelt gratitude to my supervisors, **Prof. R. K. Varshney and Prof. Dibakar Roy Chowdhury**, for granting me the invaluable opportunity to pursue my research under their guidance. Their profound inspiration, unwavering support, and insightful mentorship have been instrumental throughout my Ph.D. journey. Their extensive scientific expertise, intellectual rigor, and fervent dedication to research have significantly contributed to my development as an independent researcher, enabling me to tackle complex research problems from diverse perspectives. Working under their mentorship has been a privilege. Their ability to create a stimulating and rational scientific environment allowed me to delve deeply into my research area, thereby enhancing my analytical and scientific thinking skills.

I would also like to extend my gratitude to the SRC members, Prof. Joby Joseph, Prof. Kedar Khare, and Prof. Abhishek Dixit, for their continuous encouragement. Their insightful suggestions and feedback have assisted me in overcoming many challenges during my research work. I am also grateful to all the faculty members of the Physics Department at IIT Delhi for their invaluable advice and encouragement throughout my Ph.D. journey. Special thanks to the Dean of Academics (IIT Delhi) and the Head of the Physics Department (IIT Delhi). Moreover, I am deeply appreciative of the administration of Mahindra University (MU) for granting me permission to stay on campus and benefit from my supervisor's guidance. I am also highly thankful to the Department of Science and Technology (DST), Government of India, for providing the fellowship under the DST-INSPIRE scheme that enabled me to carry out my work during this tenure.

I cannot thank my colleagues and friends enough for their tireless and passionate support. Your daily contributions have been essential in completing this thesis and my Ph.D. I am especially grateful to Dr. Babita Bakshi, Dr. Sugeet Sunder, Dr. Nabarun Saha, Dr. Kalpak Gupta, Dr. Arnab Laha, Dr. Vikas Mishra, Dr. Subhajit Karmakar, Anjali, Geetanjali, Pratiksha, Ajay, Chandan, Parveen, Nikhil, Sayyam, Himanshu and my colleagues at Mahindra University: Arun, Soumyajyoti, Shreeya, Indu, Vaishnavi, Nityananda, Asit, Yogesh, Yogitha, Subhranshu, Chinmay, and Arpita. I also acknowledge my friends at IIT Delhi Jully, Surbhi, Swapnil, Parna di, Tina, Nikita, Shreshtha, Pialy, Rohit, Smita, Vikas, Abhishek, and Kuldeep for always being there through the highs and lows. Apart from this, I would like to thank my friends Simran, Arvinder, Jasmeet, Akanksha, Neelam, Manisha, and Diksha.

Most importantly, I would like to express my deepest gratitude to my parents, grandparents, siblings, sister-in-law, and nephew for their unwavering support, love, and gracious blessings throughout this journey. Your constant encouragement has been my motivation to move forward every day.

Finally, I would like to express my gratitude to the divine powers that have guided me through this journey.

Sukhvinder Kaur

ABSTRACT

Metamaterials, defined as artificially engineered structures with subwavelength dimensions, exhibit unique properties not observed in natural materials. These properties arise from the precise design and arrangement of their subwavelength-scale resonators. Metasurfaces, the two-dimensional counterparts of metamaterials, are composed of planar, subwavelength patterns that enable control over radiations across the electromagnetic spectrum. This unique characteristic allows metasurfaces to replace bulky optical components with thin, flat alternatives. The versatility of metamaterials has led to their application in a wide range of fields, including acoustics, mechanics, optics, and photonics. A key property of metamaterials is their scalability and the way their response is influenced by the shapes and geometry of the resonators. These features enable their utilization across the entire electromagnetic spectrum, from radio waves to visible light. The ability to tune the response of metasurfaces by manipulating their geometric configurations offers significant flexibility in their design and application, with potential implications in various industries and technologies. However, metamaterials face a notable challenge: radiative losses. These losses lead to broad line-shaped bright resonances with low Q-factors, limiting their efficiency and performance. To address this issue, researchers have utilized dark resonances, which occur through indirect excitation and are characterized by narrow line shapes with high Q-factors. Dark resonances can be excited by near-field coupling with a bright resonator or by introducing asymmetry into the structure. The introduction of asymmetry into metastructures results in properties that are not accessible in symmetric configurations, making the study of asymmetry in metasurfaces critically important. This

thesis investigates the influence of asymmetry and near-field coupling on the transmission and reflection characteristics of metasurfaces, specifically focusing on the role of behavioural, geometrical, and optical asymmetry in shaping resonances in plasmonic terahertz (THz) metamaterials.

Our study begins by demonstrating that introducing behavioural asymmetry into metasurfaces significantly enhances their sensitivity. This sensitivity enhancement results from an increased interaction volume facilitated by behavioural asymmetry, rendering these metasurfaces highly promising for applications in biosensing and material characterization, where high sensitivity is crucial for accurate detection and analysis. The investigation then extends to the effects of geometrical asymmetry on resonance characteristics, such as frequency, intensity, and Q-factor, as well as on the manipulation of electromagnetic fields at subwavelength scales. It is shown that incorporating asymmetry into the structure leads to the excitation of Fano (dark) resonances. Further coupling of these asymmetric structures results in the excitation of hybridized dark resonance states and toroidal resonances, contingent on the polarization of incident light. Additional studies on geometrical asymmetry focus on the near-field coupling between symmetric (dipole cavities) and asymmetric (split-ring resonators) structures, leading to strong coupling and enhanced transmission capabilities at new resonance frequencies. Additional investigations revealed that the position of the split ring resonator within the dipole cavity significantly affects the transmission characteristics of the structures. This positional adjustment leads to the manifestation of multi-mode surface plasmons. It is noted that geometrical asymmetry substantially influences the transmission properties of designed metasurfaces, leading to the excitation of various dark resonances such as Fano,

toroidal, multi-mode surface plasmon resonances, and hybridized dark states. These resonances have applications in biomedical sensing, filtering, and optical switching, among others.

Finally, this thesis explores optical asymmetry in metasurfaces by investigating non-Hermitian metasurface configurations, a promising approach to achieve exceptional points (EPs) and unidirectional reflectionlessness (UR). The role of near-field coupling in achieving UR is explored, highlighting the potential of this research on non-Hermitian plasmonic metasurfaces to implement futuristic THz technologies, including unidirectional cloaking and unidirectional perfect absorbers. The findings of the present thesis suggest that asymmetry and near-field coupling can significantly enhance the performance of metamaterial structures tailored specifically for THz photonics.

सारांश

मेटामटेरियल्स, जिन्हें कृत्रिम रूप से डिज़ाइन किए गए संरचनाओं के रूप में परिभाषित किया गया है एवं जिनके आयाम उप-तरंगदैर्घ्य होते हैं, प्राकृतिक सामग्रियों में न पाए जाने वाले अद्वितीय गुणधर्म प्रदर्शित करते हैं। ये गुणधर्म उनके उप-तरंगदैर्घ्य-स्तरीय अनुनादकों के सटीक डिज़ाइन और व्यवस्था से उत्पन्न होते हैं। मेटासर्फेस, मेटामटेरियल्स के द्वि-आयामी समकक्ष, समतल एवं उप-तरंगदैर्घ्य पैटर्न से बने होते हैं जो कि विद्युतचुंबकीय स्पेक्ट्रम में विकिरणों पर नियंत्रण की क्षमता प्रदान करते हैं। यह अद्वितीय विशेषता मेटासर्फेस को बड़े ऑप्टिकल घटकों को पतले, सपाट विकल्पों से बदलने की अनुमति देती है। मेटामटेरियल्स की बहुपरकारीता ने इन्हें ध्वनि विज्ञान, यांत्रिकी, ऑप्टिक्स, और फोटोनिक्स जैसे विभिन्न क्षेत्रों में उपयोग की संभावना प्रदान की है। मेटामटेरियल्स की एक प्रमुख विशेषता उनकी वृद्धि क्षमता और उनके अनुनादकों के आकार और ज्यामिति द्वारा उनकी प्रतिक्रिया पर प्रभाव है। ये विशेषताएँ इन्हें पूरे विद्युतचुंबकीय स्पेक्ट्रम में, रेडियो तरंगों से लेकर दृश्य प्रकाश तक, उपयोग के योग्य बनाती हैं। मेटासर्फेस की प्रतिक्रिया को उनके ज्यामितीय संरचना को बदलकर सुधारने की क्षमता उनके डिज़ाइन और उपयोग में महत्वपूर्ण लचीलापन प्रदान करती है, जिसका विभिन्न उद्योगों और तकनीकों पर संभावित प्रभाव पड़ सकता है। हालांकि, मेटामटेरियल्स को एक महत्वपूर्ण चुनौती का सामना करना पड़ता है: विकिरणीय हानियाँ। ये हानियाँ चौड़ी रेखा-आकृतियों वाले ब्राइट अनुनादों को जन्म देती हैं जिनके Q-फैक्टर कम होते हैं, जिससे उनकी दक्षता और प्रदर्शन सीमित हो जाता है। इस समस्या को हल करने के लिए, शोधकर्ताओं ने डार्क अनुनादों का उपयोग किया है, जो अप्रत्यक्ष उत्तेजना के माध्यम से उत्पन्न होते हैं और संकीर्ण रेखा-आकृतियों के साथ उच्च Q-फैक्टर द्वारा विशेष होते हैं। डार्क अनुनादों को

एक ब्राइट अनुनादक के साथ निकट-क्षेत्र युग्मन द्वारा या संरचना में असममिति प्रस्तुत करके उत्तेजित किया जा सकता है। मेटास्ट्रक्चर्स में असममिति की प्रस्तुति ऐसे गुणधर्मों को जन्म देती है जो सममित संरचनाओं में सुलभ नहीं होतीं, जिससे मेटासर्फेस में असममिति का अध्ययन अत्यंत महत्वपूर्ण हो जाता है। यह शोध अपवर्तन और परावर्तन विशेषताओं पर असममिति और निकट-क्षेत्र युग्मन के प्रभाव की जांच करता है, विशेष रूप से प्लास्मोनिक टेराहर्ट्ज़ (THz) मेटामटेरियल्स में अनुनादों को आकार देने में व्यावहारिक, ज्यामितीय और ऑप्टिकल असममिति की भूमिका पर ध्यान केंद्रित करता है।

हमारा अध्ययन यह दर्शाता है कि मेटासर्फेस में व्यावहारिक असममिति को पेश करने से उनकी संवेदनशीलता में महत्वपूर्ण वृद्धि होती है। यह संवेदनशीलता वृद्धि व्यावहारिक असममिति द्वारा बढ़ाए गए इंटरैक्शन आयतन के कारण होती है, जिससे ये मेटासर्फेस बायोसेंसिंग और सामग्री विश्लेषण जैसे अनुप्रयोगों के लिए अत्यधिक आशाजनक हो जाते हैं, जहां उच्च संवेदनशीलता सटीक पहचान और विश्लेषण के लिए महत्वपूर्ण होती है। इसके बाद, यह अनुसंधान ज्यामितीय असममिति के अनुनाद गुणधर्मों, जैसे कि आवृत्ति, तीव्रता, और Q-फैक्टर, पर प्रभावों के साथ-साथ उप-तरंगदैर्घ्य पैमाने पर विद्युतचुंबकीय क्षेत्रों के संचालन पर प्रभावों का अध्ययन करता है। यह दिखाया गया है कि संरचना में असममिति को शामिल करने से फैनो (डार्क) अनुनादों का उत्तेजन होता है। इन असममिति संरचनाओं के पुनः युग्मन से हाइब्रिड डार्क अनुनाद अवस्थाएँ और टोरोइडल अनुनाद उत्पन्न होते हैं, जो प्रक्षिप्त प्रकाश के ध्रुवीकरण पर निर्भर होते हैं। ज्यामितीय असममिति पर किए गए अन्य अध्ययन सममित (डायपोल कैविटीज) और असममिति (स्प्लिट-रिंग अनुनादक) संरचनाओं के बीच निकट-क्षेत्र युग्मन पर ध्यान केंद्रित करते हैं, जिससे नए अनुनाद आवृत्तियों पर मजबूत युग्मन और संवर्धित अपवर्तन जैसी क्षमताएँ प्राप्त होती हैं। विस्तृत अनुसंधान से पता चला कि डायपोल

कैविटी के भीतर स्प्लिट रिंग अनुनादक की स्थिति संरचनाओं की अपवर्तन विशेषताओं को महत्वपूर्ण रूप से प्रभावित करती है। इस स्थिति के समायोजन से मल्टी-मोड सर्फेस प्लास्मोन अनुनाद प्रकट होते हैं। यह देखा गया है कि ज्यामितीय असममिति डिज़ाइन किए गए मेटासर्फेस के अपवर्तन गुणधर्मों को महत्वपूर्ण रूप से प्रभावित करती है, जिससे विभिन्न डार्क अनुनादों जैसे कि फैनो, टोरॉइडल, मल्टी-मोड सर्फेस प्लास्मोन अनुनाद, और हाइब्रिड डार्क अवस्थाओं की उत्तेजना होती है। ये अनुनाद बायोमेडिकल सेंसिंग, फ़िल्टरिंग, और ऑप्टिकल स्विचिंग जैसे अनुप्रयोगों में उपयोगी हैं।

अंत में, इस शोध में मेटासर्फेस में ऑप्टिकल असममिति की जांच की गई है, जिसमें नॉन-हर्मिशियन मेटासर्फेस संरचना की समीक्षा की गई है, जो असाधारण बिंदुओं (EPs) और एक-तरफ़ा परावर्तनविहीनता (UR) प्राप्त करने के लिए एक आशाजनक दृष्टिकोण है। UR प्राप्त करने में निकट-क्षेत्र युग्मन की भूमिका की जांच की गई है, जिसमें एक-तरफ़ा अदृश्यता और एक-तरफ़ा परिपूर्ण अवशोषक सहित भविष्य की THz प्रौद्योगिकियों को लागू करने के लिए नॉन-हर्मिशियन प्लास्मोनिक मेटासर्फेस पर इस शोध की क्षमता पर प्रकाश डाला गया है। वर्तमान शोध के निष्कर्ष सुझाव देते हैं कि असममिति और निकट-क्षेत्र युग्मन THz फोटोनिक्स के लिए विशेष रूप से तैयार की गई मेटामटेरियल संरचनाओं की प्रदर्शन क्षमता को महत्वपूर्ण रूप से बढ़ा सकते हैं।

Table of Contents

Certificate	I
Acknowledgment	II
Abstract	IV
Table of Contents	XII
List of Figures	XVIII
List of Tables	XXXII
List of Abbreviations	XXIV
CHAPTER 1: Introduction	1
1.1. Overview of terahertz (THz) radiations and their applications	1
1.1.1 Material Characterization	2
1.1.2 Sensing and Detection	3
1.1.3 Imaging and Spectroscopy	4
1.1.4 Communication and Wireless Technology	4
1.1.5 Security and Defence	5
1.1.6 Medical Imaging and Diagnostics	7
1.2. Metasurfaces as a key component in THz wave manipulation	8
1.2.1. Historical Background	8
1.2.2. Role of Asymmetry and Near-Field Coupling in Metamaterials.....	11
1.2.2.1. Fano resonance	12

1.2.2.2.	Static Toroidal Dipole (Anapole)	15
1.2.2.3.	Dynamic Toroidal Dipole	16
1.2.2.4.	Electromagnetically Induced Transparency (EIT) .	18
1.2.2.5.	Exceptional points	20
1.2.3.	Understanding Asymmetry in Metasurfaces	23
1.2.3.1.	Behavioural Asymmetry	24
1.2.3.2.	Geometrical Asymmetry	24
1.2.3.3.	Optical Asymmetry	25
1.3.	Thesis Objectives	26
1.4.	Numerical simulations	26
1.5.	Experimental Techniques	30
1.5.1.	Device Fabrication	30
1.5.2.	Device Characterization	33
1.6.	Thesis organization	37
1.7.	Publications	42
CHAPTER 2: Behavioural Asymmetry-Driven Refractive Index Sensing		47
2.1.	Introduction	48
2.2.	Structural Configuration and Numerical Analysis	51
2.3.	Impact of Near-Field Coupling and Behavioural Asymmetry	53
2.3.1.	Intrinsic Response	53
2.3.2.	Coupled Response	56
2.4.	Dynamic Modulation of Resonance Frequencies	58

2.5. Analytical Framework: Coupled Oscillator Model	61
2.6. Refractive index sensing	63
2.7. Conclusion	67
CHAPTER 3: Geometrical Asymmetry Towards Hybrid Dark Resonance	
States	69
3.1. Introduction	70
3.2. Structural Configuration and Numerical Analysis	72
3.3. Role of Asymmetry in Structural Performance	74
3.4. Influence of Near-Field Coupling	76
3.5. Conclusion	84
CHAPTER 4: Geometrically Asymmetric Toroidal Metasurfaces for	
Avian Influenza (AI) Detection	87
4.1. Introduction	88
4.2. Structural Configuration and Numerical Analysis	90
4.3. Role of Asymmetry in Structural Performance	92
4.4. Influence of Near-Field Coupling	95
4.5. Sensing applications of designed metasurface	97
4.5.1. Thin-film sensing	97
4.5.2. Refractive-index sensing	100
4.6. Conclusion	106
CHAPTER 5: Phase Modulation in Asymmetric Metasurfaces	109
5.1. Introduction	110

5.2. Structural Configuration and Numerical Analysis	114
5.3. Coupling Dynamics Between Symmetric Dipole Cavities and Asymmetric Split Ring Resonators	116
5.3.1 Intrinsic Response of the Dipole Cavity and SRR	116
5.3.2 Electromagnetic Response of Coupled Hybrid Cavity	117
5.3.2.1. For gap (g) > 3 μm	117
5.3.2.2. For gap $2.3 \leq g \leq 3 \mu m$	125
5.3.2.3. For gap (g) < 2.3 μm	128
5.4. Conclusion	131
CHAPTER 6: Geometrical Asymmetry Mediated Multi-Mode Surface Plasmon Hybridizations	133
6.1. Introduction	134
6.2. Structural Configuration and Numerical Analysis	137
6.3. Coupling Dynamics of Cavity and SRR and Effect of Asymmetry	139
6.3.1. Effect of Near Field Coupling	139
6.3.2. Effect of Asymmetry	142
6.4. Conclusion	150
CHAPTER 7: Exceptional Points in Non-Hermitian Plasmonic Metasurfaces	153
7.1. Introduction	154
7.2. Structural Configuration and Numerical Analysis	157
7.3. Realizing a non-Hermitian Metasurface System	159

7.3.1. Intrinsic Response of Split Ring Resonator (SRR)	159
7.3.2. Effect of Orthogonal Near-Field Coupling	161
7.4. Conclusion	176
CHAPTER 8: Summary and Future Research Opportunities	179
8.1. Summary	180
8.2. Future Research Opportunities	181
References	185

List of Figures

Figure 1.1. (a) Phase diagram in damping constant (γ_1 & γ_2) plane illustrating the various regimes conducive to different resonance excitations, including Fano resonance, electromagnetically induced transparency (EIT), the Kerker effect, parity-time (PT) symmetry breaking (both sustaining and breaking), and strong and weak coupling regimes. An inset provides a schematic representation of the coupled damped oscillator model [adapted from (Limonov et al., 2017)]; (b) The top spectra represent the amplitude of the resonator in a coupled system, exhibiting two peaks: one with a symmetric line-shape and the other with an asymmetric line-shape. The resonance with the asymmetric line-shape is identified as a Fano resonance. The bottom spectra illustrate the corresponding phase behaviour of the system, showing the phase change at these resonances [adapted from (Joe et al., 2006)]. 14

Figure 1.2. 3D schematic illustrating the manifestation of anapole through the destructive interference of electric and toroidal dipoles with the same radiation pattern [adapted from (Baryshnikova et al., 2019)]. .. 15

Figure 1.3. A 3D schematic illustrating (a) an electric dipole formed by a pair of oppositely charged particles, (b) a magnetic dipole created by a current j flowing in a loop, and (c) a toroidal dipole generated by a

current j flowing along the surface of a torus [adapted from (Kaelberer et al., 2010)]. 18

Figure 1.4. (a) Prototype atomic system for EIT with the probe field frequency ω_p and ω_c being the coupling frequency. The field detuning from atomic resonance is represented by $\Delta_1 = \omega_{31} - \omega_p$ and $\Delta_2 = \omega_{32} - \omega_p$, while Δ_{ik} represents the decay from the state $|i\rangle$ to state $|k\rangle$; (b) The EIT system with resonant coupling (solid line) with the top (bottom) figure representing the imaginary (real) part of the susceptibility, characterizing the absorption (refractive index) of the medium. The dashed line shows the susceptibility as a function of frequency [adapted from (Fleischhauer et al., 2005)]. 19

Figure 1.5. (a) Illustration of PT- symmetry in Fabry-Perot resonator; (b) the eigenvalues of the scattering matrix for PT-symmetric resonator [adapted from (Miri & Alù, 2019)]. 21

Figure 1.6. Snapshot from CST illustrating: (a) the mesh formation in the designed metastructure, (b) the applied boundary conditions, (c) the control parameters for the frequency domain solver, and (d) the material library. 28

Figure 1.7. 3D schematic illustrating the steps involved in the fabrication process. 31

Figure 1.8. 3D Schematic depicting THz (a) generation and (b) detection. [adapted from (J. Li & Li, 2020)]. 34

Figure 1.9. (a) Schematic of THz-TDS setup [adapted from (L. Wei et al., 2018)], (b) Camera image of the THz- TDS setup. 35

Figure 2.1. The schematic of the designed metamaterial. (a) An artistic illustration depicting the interaction between the incident THz radiation and an infinite array of broadside-coupled graphene metamaterials, (b) A perspective view illustrating the designed unit cell, featuring two broadside-coupled “plus”-shaped resonators separated by a sub-wavelength scale spacer, highlighting various parameters $P = 22 \mu m, l = 20 \mu m, w = 4 \mu m, t_s = 50 \mu m, t_g = 1 \text{ nm}$, (c) A side (xz) view of the designed unit cell, highlighting the spacer with thickness “ d ”. 52

Figure 2.2. Transmission spectra illustrating the shifting of resonance on varying the spacer thicknesses ‘ d ’ for intrinsic (a) bottom and (b) top resonators; Transmission spectra for (c) behavioural symmetric and (d) behavioural asymmetric coupled resonators; Electric field distribution inside the cavity for spacer thickness (e) $1 \mu m$ (f) $2 \mu m$, and (g) $6 \mu m$ 54

Figure 2.3. Transmission spectra for the (a) bottom and (b) top resonators as the graphene Fermi energy varied; (c) 2D colour plot detailing transmission behaviour for varying Fermi Energy and a fixed spacer thickness of $2 \mu m$; (d) resonance frequency split (Δf) across

different Fermi energy levels for both coupled and intrinsic 60
structures.

Figure 2.4. Comparison between analytical and simulated transmission spectra for Fermi energy of 0.4 (a) and 0.8 (b) eV, with a constant spacer thickness $d = 2 \mu m$ 62

Figure 2.5. (a) 2D colour plot depicting the shifting of resonance on varying the refractive index of the analyte with a thickness of $2 \mu m$, (b) Change in the sensitivity (THz/RIU) of the designed metasurface with the refractive index analyte, (c) transmission spectra for varying loss rates ($\tan \delta$); Electric field distribution inside the cavity for spacer refractive index (d) 1, (e) 1.5, (f) 1.8, (g) 2.1, and (h) 2.4. 65

Figure 3.1. (a) A 3D artistic illustration depicting the interaction between the incident THz radiation and an infinite array of broadside-coupled graphene metamaterials; (b) A Front view of the designed unit cell featuring two asymmetric split ring resonators placed in a mirrored configuration, highlighting various parameters $P_x = 150 \mu m, P_y = 75 \mu m, l = 60 \mu m, w = 7 \mu m, a = \text{asymmetry (variable)}, d = \text{separation (variable)}$; (c) A side (xz) View of the designed unit cell, highlighting the thickness of the substrate $t_s = 25 \mu m$, and resonator $t = 200 \text{ nm}$ 73

Figure 3.2. (a) Optical microscopic image of the intrinsic asymmetric SRR, (b) Transmission spectra of intrinsic metastructure for varying

asymmetry parameters a ; Comparison between simulated and experimental data for (c) $a = 10 \mu m$ and (d) $a = 20 \mu m$. Surface current distribution for $a = 20 \mu m$ at (e) $f_1 = 0.43$ THz, (f) $f_2 = 0.95$ THz, and (g) $f_3 = 1.21$ THz. 75

Figure 3.3. Optical microscopic images for coupled metastructure for (a) $a = 10 \mu m$ and (b) $a = 20 \mu m$; Simulated and experimental transmission spectra for varying asymmetry parameter (a) and separation between two SRRs (d): (c) $a = 10 \mu m, d = 3 \mu m$, (d) $a = 10 \mu m, d = 8 \mu m$, (e) $a = 10 \mu m, d = 15 \mu m$, (f) $a = 20 \mu m, d = 3 \mu m$, (g) $a = 20 \mu m, d = 8 \mu m$, (h) $a = 20 \mu m, d = 15 \mu m$ 78

Figure 3.4. 2D color plot depicting the shifting of the resonance on varying the inter-resonator keeping fixed asymmetry of $a = 20 \mu m$ and a table of Q-factor for f_I and f_{II} for different separation and asymmetry parameters. 80

Figure 3.5. Surface current distribution for coupled SRRs with asymmetry parameter (a) = $10 \mu m$ and separation between two SRRs (d) = $15 \mu m$; (a) $f_I = 0.48$ THz, (b) $f_{II} = 0.57$ THz, (c) $f_{III} = 1.08$ THz, (d) $f_{IV} = 1.17$ THz; and corresponding electric field distribution: (e) $f_I = 0.48$ THz, (f) $f_{II} = 0.57$ THz, (g) $f_{III} = 1.08$ THz, (h) $f_{IV} = 1.17$ THz. 82

Figure 4.1. (a) Perspective view of the designed unit cell featuring two asymmetric split ring resonators placed in a mirrored configuration, highlighting various parameters $P_x = 150 \mu m, P_y = 75 \mu m, l =$

60 μm , $w = 7 \mu\text{m}$, $a = \text{asymmetry (variable)}$, $d =$
separation (variable); (b) A 3D artistic illustration depicting the
excitation of toroidal dipoles in planar metasurfaces. 91

Figure 4.2. Optical microscopic image of an intrinsic dual-gap split ring
resonator, illustrating the introduction of asymmetry by shifting the
top gap relative to the bottom gap. 92

Figure 4.3. (a) Transmission spectra of intrinsic split ring resonators with
varying asymmetry; (b) Enlarged view of the spectra illustrating the
reshaping of resonances. Comparison between experimental and
simulated transmission spectra for (c) $a = 10 \mu\text{m}$ and (d) $a =$
20 μm ; surface current distribution corresponding to $a = 20 \mu\text{m}$ at
(e) $f_I = 0.426 \text{ THz}$ and (f) $f_{II} = 0.618 \text{ THz}$; corresponding
electric field distribution at (g) $f_I = 0.426 \text{ THz}$ and (h) $f_{II} =$
0.618 THz. 94

Figure 4.4. (a) Optical microscopic image of coupled metastructures along with
unit cell in the inset; (b) Experimental and simulated transmission
spectra for coupled structure for $a = 20 \mu\text{m}$; surface current
distribution corresponding to the frequency (c) $f_I = 0.411 \text{ THz}$ and
(d) $f_{II} 0.71 \text{ THz}$; and electric field distributions corresponding to (e)
 $f_I = 0.411 \text{ THz}$ and (f) $f_{II} 0.71 \text{ THz}$ 97

Figure 4.5. (a) Simulated and (b) experimental transmission spectra showcasing
the shift in resonance frequency after placing the analyte on the top

of the designed metasurface; (c) Simulated transmission spectra illustrating the resonance frequency shift with varying analyte thickness; (d) Simulated frequency shift of the toroidal resonance corresponding to different analyte thicknesses (inset figure of merit derived from simulated data for toroidal resonance across various analyte thicknesses). 99

Figure 4.6. (a) Transmission spectra depicting the shift in resonance frequency for varying the refractive index of analyte and (b) Toroidal resonance frequency shift with varying refractive index of the analyte. 101

Figure 4.7. (a) 3D schematic of the proposed virus detection scheme; Simulated transmission spectra depicting the change in (b) spectral response for various β values at constant $\alpha = 1.2$; (c) resonance frequency for various α values at constant $\beta = 1.4$ 103

Figure 4.8. Transmission spectra depicting the resonance shift for various analytes (bare sample, photoresist, H5N2, and H9N2). 104

Figure 5.1. (a) 3D Artistic illustration of coupled hybrid cavity portraying the interaction with incident terahertz radiation. (b) A perspective view of the designed unit cell featuring split ring resonators placed in the vicinity of the dipole cavity, highlighting various parameters $P_x = 83 \mu m, P_y = 83 \mu m, h = 40 \mu m, l = 20 \mu m, w = 5 \mu m,$ and $g = variable,$ (c) A side (xz) View of the designed unit cell,

highlighting the thickness of the substrate $t_s = 25 \mu m$, and resonator $t = 200 nm$, (d) Optical microscopic image portraying the coupling of the intrinsic split ring resonator and dipole cavity; Optical microscopic images of the unit cell with (e) $g = 3 \mu m$, (f) $g = 6 \mu m$, (g) $g = 10 \mu m$ 115

Figure 5.2. Comparison between the experimental and simulated transmission spectra for (a) split ring resonator (b) dipole cavity. 116

Figure 5.3. Comparison between the experimental and simulated transmission spectra of the hybrid cavity for (a) y –polarized (b) x –polarized THz incidence. 118

Figure 5.4. Comparison between the experimental and simulated transmission spectra of the hybrid cavity for (a) $g = 3 \mu m$, (b) $g = 4 \mu m$, (c) $g = 6 \mu m$, and (d) $g = 10 \mu m$ 119

Figure 5.5. Surface current distributions corresponding to (a) Split Ring Resonator, (b) Dipole cavity, and for coupled hybrid cavity corresponding to gap width $g = 10 \mu m$ at (c) $f_{cavity} = 1.03 THz$, (d) $f_{SRR} = 1.10 THz$, (e) $f_{WA} = 1.05 THz$, (f) $f_{SRR-dip} = 1.3 THz$, and surface current corresponding to (g) $f_{cavity-SRR} = 1.00 THz$, (h) $f_{SRR-dip} = 1.05 THz$ corresponding to $g = 3 \mu m$; Magnetic field distribution for coupled hybrid cavity corresponding to gap width $g = 10 \mu m$ at (i) $f_{cavity} = 1.03 THz$, (j) $f_{WA} = 1.05 THz$,

(k) $f_{SRR} = 1.10 \text{ THz}$, and magnetic field distribution corresponding to (l) $f_{cavity-SRR} = 1.00 \text{ THz}$, corresponding to $g = 3 \mu\text{m}$ 123

Figure 5.6. (a) Variation in resonance frequency position of both the peaks and dip with gap size; (b) Transmission spectra for shifting the SRR gap position along the y-axis, (c) Transmission spectra of coupled and uncoupled structure for gap size $g = 3 \mu\text{m}$; (d) Transmission spectra corresponding to different periodicity for $g = 3 \mu\text{m}$ 127

Figure 5.7. (a) Transmission spectra for coupled hybrid structure corresponding to different gap sizes for $g \leq 3 \mu\text{m}$; (b) Transmission spectra of coupled and uncoupled structure for gap size $g = 1 \mu\text{m}$; Surface current distribution for gap $g = 1 \mu\text{m}$: (c) $f_{SRR} = 0.96 \text{ THz}$, (d) $f_{SRR-dip} = 1.02 \text{ THz}$, (e) $f_{cavity} = 1.04 \text{ THz}$, (f) $f_{WA} = 1.07 \text{ THz}$; E-field distribution for $g = 1 \mu\text{m}$: (g) $f_{SRR} = 0.96 \text{ THz}$, (h) $f_{SRR-dip} = 1.02 \text{ THz}$, (i) $f_{cavity} = 1.04 \text{ THz}$, (j) $f_{WA} = 1.07 \text{ THz}$ 129

Figure 6.1. (a) 3D artistic view of the structure depicting the interaction with THz radiations, (b) Perspective view of the unit cell of the proposed structure having geometrical parameters $P_x = P_y = 83 \mu\text{m}$, $h = 40 \mu\text{m}$, $l = 20 \mu\text{m}$, $w = 5.5 \mu\text{m}$, $g = 3 \mu\text{m}$; (c) side view of the designed unit cell; Optical microscopic image of uncoupled (d) dipole cavity, (e) SRR, and the coupled structure depicting the displaced positions of SRR in (f) $+x$ - direction, (g) $-x$ - direction, and (h) $+y$ - direction. 138

Figure 6.2. Simulated and experimental transmission spectra for (a) dipole cavity, (b) split ring resonator, and (c) coupled hybrid cavity; (d) Mode hybridization scheme for the coupling of cavity and SRR; Surface current distribution for (e) P_2 ($f = 1.0278$ THz) and (f) P_1 ($f = 1.1574$ THz).	139
Figure 6.3. Experimental and simulated transmission spectra for (a) $\Delta x = +5 \mu\text{m}$, (b) $\Delta x = +7 \mu\text{m}$, (c) $\Delta x = -5 \mu\text{m}$, (d) $\Delta x = -7 \mu\text{m}$; (e) $\Delta y = +5 \mu\text{m}$, and (f) $\Delta y = +7 \mu\text{m}$	143
Figure 6.4. Surface current distribution for displacement in y - direction $\Delta y = +7 \mu\text{m}$ at (a) $f_{P_2} = 1.0098$ THz, (b) $f_{P_3} = 1.1088$ THz, (c) $f_{P_1} = 1.1574$ THz; electric field distribution at (d) $f_{P_2} = 1.0098$ THz, (e) $f_{P_3} = 1.1088$ THz, (f) $f_{P_1} = 1.1574$ THz.	145
Figure 6.5. 3-state mode hybridization scheme depicting the coupling between the cavity and SRR modes.	147
Figure 6.6. 2D colour plot depicting the detuning of the resonances for the displacements of SRR along the (a) x - and (b) y - directions within the dipole cavity.	149
Figure 7.1. (a) 3D illustration portraying the interaction of incident THz radiation with designed metasurface, (b) unit cell of the designed metastructure representing various parameters being $P_x = 120 \mu\text{m}$, $P_y = 60 \mu\text{m}$, $l = 40 \mu\text{m}$, $g = 3 \mu\text{m}$, $w = 6 \mu\text{m}$, $t_s = 25 \mu\text{m}$, $d = \text{variable}$; (c) schematic of two port systems	

showcasing the incident, reflected, and transmitted waves from both the ports; optical microscopic images of (d) intrinsic resonator and (e-i) coupled-resonators with varying separations between the near-field coupled resonators: (e) $d = 0 \mu\text{m}$ (f) $d = 1 \mu\text{m}$ (g) $d = 3 \mu\text{m}$ (h) $d = 12 \mu\text{m}$ (i) $d = 18 \mu\text{m}$ 158

Figure 7.2. (a, c) Simulated and (b, d) analytical reflection spectra for (a, b) y -polarized and (c, d) x -polarized THz radiation; (e, g) Simulated and (f, h) experimental transmission spectra for (e, f) y -polarized and (g, h) x -polarized THz radiation. 159

Figure 7.3. Reflection spectra for different conductivity (losses) of SRR material under (a) Forward and (b) Backward incidents for x -polarized light. 161

Figure 7.4. (a) Reflection spectra for the coupled metastructure under both forward and backward incidences of THz light for y -polarization; (b) Real and (c) Imaginary parts of eigenvalues and (d) asymmetry factor for y -polarized incidence; (e) Reflection spectra for the coupled metastructure under both forward and backward incidences of THz light for x -polarization; (f) Real and (g) Imaginary parts of eigenvalues and (h) asymmetry factor for x -polarized incidence. 166

Figure 7.5. Electric field distribution along (a) $x - y$ plane at $z = 25.2 \mu m$, (b) $x - z$ plane at $y = 15 \mu m$; (c) variation of the electric field inside the dielectric substrate along z -axis. 168

Figure 7.6. Simulated reflection spectra under forward and backward incidences of $y -$ polarized THz light for separation (a) $d = 1 \mu m$, (b) $d = 3 \mu m$, (c) $d = 12 \mu m$, (d) $d = 18 \mu m$; Analytical reflection spectra under forward and backward incidences of $y -$ polarized THz light for separation (e) $d = 1 \mu m$, (f) $d = 3 \mu m$, (g) $d = 12 \mu m$, (h) $d = 18 \mu m$ 168

Figure 7.7. Simulated transmission spectra under forward and backward incidences of $y -$ polarized THz light for separation (a) $d = 1 \mu m$, (b) $d = 3 \mu m$, (c) $d = 12 \mu m$, (d) $d = 18 \mu m$; (b) Experimental transmission spectra under forward and backward incidences of THz light for separation (e) $d = 1 \mu m$, (f) $d = 3 \mu m$, (g) $d = 12 \mu m$, (h) $d = 18 \mu m$ 170

Figure 7.8. Simulated reflection spectra under forward and backward incidences of $x -$ polarized THz light for separation (a) $d = 1 \mu m$, (b) $d = 3 \mu m$, (c) $d = 12 \mu m$, (d) $d = 18 \mu m$; (b) Analytical reflection spectra under forward and backward incidences of THz light for separation (e) $d = 1 \mu m$, (f) $d = 3 \mu m$, (g) $d = 12 \mu m$, (h) $d = 18 \mu m$ 171

Figure 7.9. (a) Real, (b) imaginary parts of eigenvalues, and (c) Asymmetry factor for y - polarized THz probe; (d) Real, (e) imaginary parts of eigenvalues, and (f) Asymmetry factor for x - polarized THz probe for varying the separation (d). 174

List of Tables

Table 2.1	Parameters for the theoretical model for $d = 2 \mu\text{m}$ and Fermi energy 0.4 and 0.8 eV.	63
Table 2.2	Table 2.2. Comparison of the reported sensitivity with previous studies.	66
Table 4.1	Total protein concentration and relative complex refractive index of Avian Influenza virus subtypes.	102

List of Abbreviations

ASRR	Asymmetric Split Ring Resonator
AI	Avian Influenza
BR	Bottom Resonator
CRI	Complex Refractive Index
CST	Computer Simulation Technology
DI	Deionized
EIT	Electromagnetically Induced Transparency
EP	Exceptional Points
FFT	Fast Fourier Transformation
FEM	Finite Element Method
FIT	Finite Integration Technique
IR	Infrared
LHM	Left-handed Materials
LSPR	Localized Surface Plasmon Resonances
MoM	Method of Moments
PT	Parity-Time
PCA	Photoconductive Antenna
PR	Photoresist
RF	Radio Frequency
RIU	Refractive Index Unit
rpm	Rotations per minute

SRR	Split Ring Resonator
SP	Surface Plasmon
SPR	Surface Plasmon Resonance
THz	Terahertz
THz-TDS	Terahertz Time Domain Spectroscopy
TW	Thin Wire
TR	Top Resonator
UV	Ultraviolet
UR	Unidirectional Reflectionlessness
WA	Wood's Anomaly